

Article

Effect of Surfactant Dynamics on Flow Patterns Inside Drops Moving in Rectangular Microfluidic Channels

Nina M. Kovalchuk *  and Mark J. H. Simmons

School of Chemical Engineering, University of Birmingham, Edgbaston, Birmingham B15 2TT, UK; M.J.Simmons@bham.ac.uk

* Correspondence: N.Kovalchuk@bham.ac.uk

Abstract: Drops contained in an immiscible liquid phase are attractive as microreactors, enabling sound statistical analysis of reactions performed on ensembles of samples in a microfluidic device. Many applications have specific requirements for the values of local shear stress inside the drops and, thus, knowledge of the flow field is required. This is complicated in commonly used rectangular channels by the flow of the continuous phase in the corners, which also affects the flow inside the drops. In addition, a number of chemical species are present inside the drops, of which some may be surface-active. This work presents a novel experimental study of the flow fields of drops moving in a rectangular microfluidic channel when a surfactant is added to the dispersed phase. Four surfactants with different surface activities are used. Flow fields are measured using Ghost Particle Velocimetry, carried out at different channel depths to account for the 3-D flow structure. It is shown that the effect of the surfactant depends on the characteristic adsorption time. For fast-equilibrating surfactants with a characteristic time scale of adsorption that is much smaller than the characteristic time of surface deformation, this effect is related only to the decrease in interfacial tension, and can be accounted for by the change in capillary number. For slowly equilibrating surfactants, Marangoni stresses accelerate the corner flow, which changes the flow patterns inside the drop considerably.

Keywords: multiphase flow; drop microfluidics; rectangular channel; flow pattern; corner flow; surfactant dynamics; aqueous/oil interface; Langmuir isotherm parameters; characteristic adsorption time



Citation: Kovalchuk, N.M.; Simmons, M.J.H. Effect of Surfactant Dynamics on Flow Patterns Inside Drops Moving in Rectangular Microfluidic Channels. *Colloids Interfaces* **2021**, *5*, 40. <https://doi.org/10.3390/colloids5030040>

Academic Editors: Giuseppe Loglio and Reinhard Miller

Received: 23 June 2021
Accepted: 23 July 2021
Published: 2 August 2021

Publisher's Note: MDPI stays neutral with regard to jurisdictional claims in published maps and institutional affiliations.



Copyright: © 2021 by the authors. Licensee MDPI, Basel, Switzerland. This article is an open access article distributed under the terms and conditions of the Creative Commons Attribution (CC BY) license (<https://creativecommons.org/licenses/by/4.0/>).

1. Introduction

Using microfluidic drops as microreactors is a rapidly developing area that enables reaction studies and optimization using a statistically relevant number of reactors. This platform enables tightly controlled conditions, with minimal cross-contamination and advective dispersion, whilst using small amounts of reagents [1]. This enables a considerable reduction of the ecological impact of research and development, and potentially increases the rate of production of new formulations. Drop microreactors have been successfully used for activities including the measurement of kinetic constants of chemical and biochemical reactions [2–4], drug–protein association constants [5], cell screening [6–8], synthesis of nanoparticles [9–11] and hydrogel particles [12–14].

Precise control of flow fields, shear stresses and mixing inside the micro-reactors are essential for many applications. The flow pattern is complicated, due to the combined action of shear stresses from the wall and coupling of the flow fields between the dispersed and continuous phases, even in simple geometries [15]. A large number of microfluidic devices have a rectangular cross-section, in particular those made by soft lithography [16]. This causes additional complications because the continuous phase can move more slowly in thin films near the channel walls and much faster in the corners (gutters), due to different hydrodynamic resistances. Numerical simulations show that the presence of the corner flow results in the smaller deformation and higher velocity of the drop in a square channel,

compared with a cylindrical channel [17]. Theoretical analysis [18,19], carried out on a long air bubble moving in a rectangular channel, predicts that the corner flow is dominant at small capillary numbers (Ca), whereas plug flow is expected at large capillary numbers. The same conclusion was made for a long drop moving under similar conditions using numerical simulations [20].

Presentation of the first evidence of a corner flow exceeding the drop velocity was given in [21], where the movement of bubbles in water inside a microfluidic channel with rectangular cross-section was studied at values of Ca of $O(10^{-3})$. The length of the bubbles studied was 3 to 10 times the channel width. It was observed in [21] that a debris particle, used as a tracer, moved through the corner gutter from behind the rear part of a bubble, and then appeared at the front of the bubble.

The main method used to study flow fields in microfluidic drops is micro-particle image velocimetry (μ -PIV) [22–28]. In most studies, flow fields were measured at the middle plane of the channel. A thorough 3-D reconstruction of flow patterns inside a drop moving through a rectangular channel (with an aspect ratio of 0.58) was carried out in [23], using confocal μ -PIV when the ratio of dispersed phase viscosity, μ_d , to continuous phase viscosity, μ_c , was equal to $\mu_d/\mu_c = 0.23$. Flow fields were measured for several horizontal cross-sections and then the vertical components of the flow velocity were calculated from the continuity equation. The flow was found to have a complicated 3-D structure, with liquid near the walls moving more slowly than the drop, whereas the liquid in contact with continuous phase in the corners moved faster than the drop. The methodology was developed further using multicolor confocal micro-PIV [24], which enabled simultaneous measurement of flow fields in both phases. The generalized distribution of surface stresses (and surface flows) in the presence of corner flow is shown in Figure 1 [28].

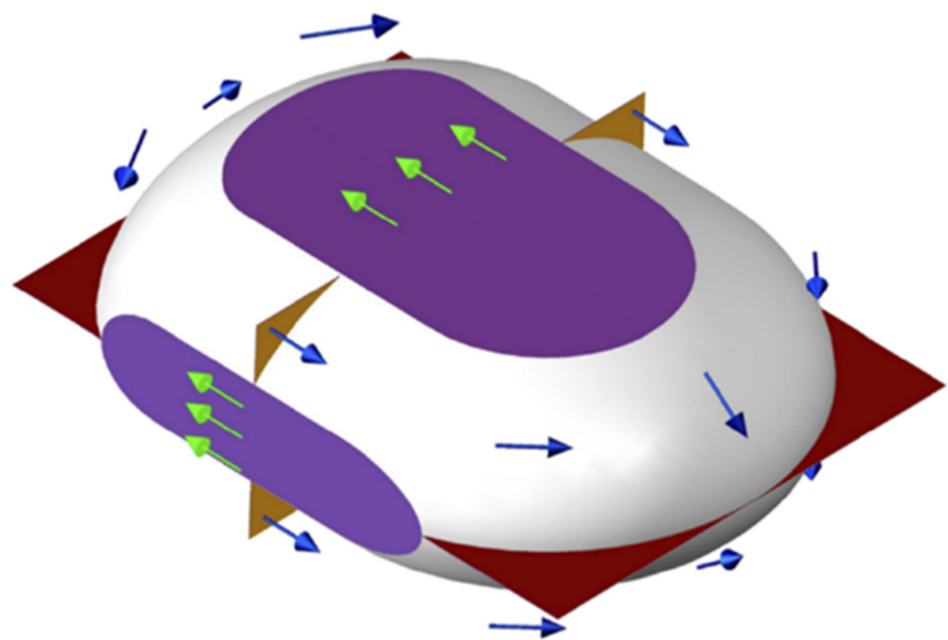


Figure 1. Flow patterns/stresses on the surface of drop moving in a rectangular channel. Reprinted from a study by Li et al. [28]. Copyright 2020, with permission from AIP Publishing.

3-D reconstruction of the flow in both phases was carried out in [25] for a drop moving inside a near-square channel with a viscous dispersed phase (viscosity ratio 2.625). Under these conditions, the velocity of the surface flow in contact with both films and corner gutters was smaller than the drop velocity, with the velocity within the films being smaller than within the gutters. In the middle plane of the channel, the flow field was composed of two symmetrical convective rolls in the central part of the drop, due to interaction with thin films of the continuous phase near the walls. Two pairs of smaller vortices were present at

the front and the rear of the drop, due to interaction with the flow in the slugs of continuous phase separating the drops.

Comparison of the results between [23–25] clearly indicates that the channel aspect ratio and viscosity ratio are important parameters affecting the flow patterns inside the drop. Different flow patterns were observed in [22] using a channel with an aspect ratio of 0.75 at the viscosity ratios of $\mu_d/\mu_c = 0.12$ and 0.78. Other important parameters are the drop size [29], the volume fraction of the dispersed phase [30], and capillary number.

The effect of the capillary number on the velocity of a single drop with a length of 0.8 to 16 times the channel width, moving in a square channel, was studied in [26] over a range of viscosity ratios. It was found that, at small capillary numbers, the flow field in the middle plane comprised two symmetrical convective vortices occupying the whole length of the drop, whereas, at large capillary numbers, a flow pattern comprising three pairs of convective rolls was found, similar to that observed in [25]. The transition was accompanied by a discontinuity in drop velocity. The threshold value of the capillary number was $O(10^{-3})$ and increased with a corresponding increase in the viscosity ratio. It was suggested in [26] that transition does not take place if the viscosity ratio is greater than unity. Two transitions in flow topology in the middle plane of a drop were found in the case of a channel with an aspect ratio of 0.67, at values of $Ca \sim 10^{-3}$ and $Ca \sim 10^{-2}$ [27]. Similar to the square channel, threshold values of the capillary number increased with an increase in dispersed phase viscosity, but the observed flow patterns were different. At small values of the capillary number, the flow comprised two symmetrical vortices near the walls and two pairs of vortices in the central part of the drop. For intermediate Ca , the two vortices near the walls remained unchanged, but the flow in the central part did not show recirculation patterns, being instead part of a 3-D flow pattern. Flow at large Ca was characterized by a considerable increase in velocity in the central part of the drop [27].

The presence of a surfactant further complicates matters. Firstly, a surfactant reduces interfacial tension between the phases, resulting in increased drop deformability that changes the drop shape and thickness of the continuous phase films. The film thickness is determined by the balance of the drag force from the channel wall and the capillary pressure between the dispersed and continuous phase: the larger the value of capillary pressure, the thinner the film [31]. Therefore, a considerable decrease in interfacial tension due to surfactant addition results in a considerable increase in film thickness. Secondly, due to the characteristic timescales in microfluidics, the acting interfacial tension can be far from equilibrium. Thirdly, shear stresses imposed by the continuous phase can result in surfactant redistribution and partial or complete retardation of the interface (Marangoni stresses), changing the flow pattern at the interface and inside the drop. The essential effect of Marangoni stresses on drop motion in a square channel was found in numerical simulations for non-soluble [32] and soluble [33] surfactants.

The effect of surfactant redistribution over the interface is well-documented regarding an air bubble rising in contaminated water [34–36]. As surfactant is swept by the flow from the front part of the drop to the rear, this can result in partial or full surface retardation and dependence of the bubble terminal velocity on surfactant concentration. A much more complicated scenario is observed for a microfluidic drop moving in a rectangular microfluidic channel. In this case, the surface stresses from the continuous phase are strongly non-uniform, and surfactant is always swept to the rear of the drop by the flow in the liquid films near channel walls but can be forced toward the front by the continuous phase, bypassing the drop through the liquid corners.

It was shown in [21] that the presence of surfactant in the continuous phase can considerably slow down bubble motion at moderate surfactant concentrations. This deceleration was ascribed to retardation of the bubble surface, similar to the unconfined case. The sweeping of surfactant to the rear of a long drop moving in a rectangular channel was demonstrated in [37] by imaging a fluorescent surfactant.

In most studies on microfluidic drops or bubbles moving in a rectangular channel, the surfactant was dissolved in the continuous phase [21,22,27,28,37] with the aim of drop

stabilization and comparison between the surfactant-free and surfactant-laden case. Usually, surfactant concentration was fixed in these studies. In microfluidic reactors, surfactant concentrations can vary over a broad range. To understand the effect of surfactants in detail, several surfactants with different surface activity over a range of concentrations must be studied. As identified in the above review, the behavior of surfactants within the confinement of a drop can be very different from a surfactant in the continuous phase. The detailed examination of the effect of surfactant added to dispersed phase on the flow pattern inside this phase is the focus of this work. In this paper, the flow patterns inside the dispersed phase are measured and compared for surfactant-free and surfactant-laden drops. Two ionic and two non-ionic surfactants are studied, over a range of concentrations below and above the critical micelle concentration (CMC).

2. Materials and Methods

The continuous phase used in this study was silicone oil, SO, (Sigma Aldrich, Salisbury, UK, product number 378356). The dispersed phase used was a 52:48 *w:w* mixture of ultrapure HPLC-grade glycerol (Alfa Aesar, Ward Hill, MA, USA) and double-distilled water obtained from a water still (Aquatron A 4000 D, Stuart, FL, USA). Glycerol was added to the dispersed phase to match the refractive index with the continuous phase, to prevent optical distortions at the interface. The properties of liquid phases are listed in Table 1. The uncertainty in interfacial tension is due to variations of the room temperature of 22 ± 3 °C.

Table 1. Properties of continuous and dispersed phases.

	Density kg/m ³	Viscosity mPa·s	Interfacial Tension, mN/m
Continuous phase: silicone oil	960	48	
Dispersed phase: 52:48 <i>w:w</i> glycerol/water	1133	6	33.4 ± 0.4

Surfactants, decyltrimethylammonium bromide, C₁₀TAB, (99%, Acros Organics, M = 280.29 g/mol), dodecyltrimethylammonium bromide, C₁₂TAB, (99%, Acros Organics, M = 308.34 g/mol), Triton X-100, TX-100, (laboratory grade, Sigma Aldrich, product number X100, M ~ 625 g/mol) and Tween 20 (BioXtra, Sigma Aldrich, product number P7949, M ~ 1228 g/mol) were dissolved in the dispersed phase. The range of concentrations investigated was between 0.1 to 10 times the CMC. The surfactant presence did not affect the viscosity of the dispersed phase in the studied concentration range.

Interfacial tension was measured using a force tensiometer Attension Sigma 701 (Biolin Scientific, Espoo, Finland), equipped with a platinum Du Noüy ring. The measurement was carried out for at least 1 h to make sure that the equilibrium interfacial tension was achieved. The readings were taken every 2 min for measurement, up to 4 h, and every 3 or 5 min for longer measurements, to minimize the interface disturbance. Due to the very slow equilibration rate, solutions of Tween 20 were agitated using a magnetic stirrer bar (Fisher, diameter 4.5 mm, length 15 mm), at 30% of the maximum speed allowed by the tensiometer during the measurement. Before each measurement, the surface tension of water was measured under stirring with the same stirrer bar for 1 h to ensure the cleanliness of the glassware and stirrer bar. To eliminate the effect of stirring on the results, the stirring was switched off and the measurement proceeded without stirring for another hour. The parameters of the Langmuir isotherm were extracted from the dependence of interfacial tension on concentration, using the free software IsoFit [38,39] (see Section 3.2 below). The dynamic surface tension of the surfactant solutions was measured using a maximum bubble pressure tensiometer BPA-1S (Sinterface, Berlin, Germany).

The mold for the microfluidic device was prepared by photolithography using the negative photoresist SU-8 2075. To create a device by soft lithography, polydimethylsiloxane, PDMS, (SYLGARD 184, Dow Corning) was mixed with the curing agent (10:1 *w:w*), cast

on the mold, degassed in a vacuum chamber, cured at 70 °C for 3 h, and left overnight for equilibration. Afterward, the replica was pulled off the mold and, after punching holes for tubing, was sealed by a glass slide with a spin-coated and cured surface layer of PDMS of the same composition. To get reliable contact, both parts were treated by corona discharge for 2 min before sealing. The device was hydrophobized by filling it with Aquapel for 5 min at 80 °C. The residuals of Aquapel were removed by nitrogen stream.

A schematic of the microfluidic device is shown in Figure 2a. The rectangular channels have a width, $W = 346 \pm 3 \mu\text{m}$, and a height, $H = 167 \pm 3 \mu\text{m}$, with the aspect ratio, $A = H/W = 0.48$. Considering that PDMS is prone to swelling in silicone oil, the device was kept filled with continuous phase for 1 week prior to use, but there was still a rather slow decrease in the channel size afterward, reflected in the given deviations for H and W .

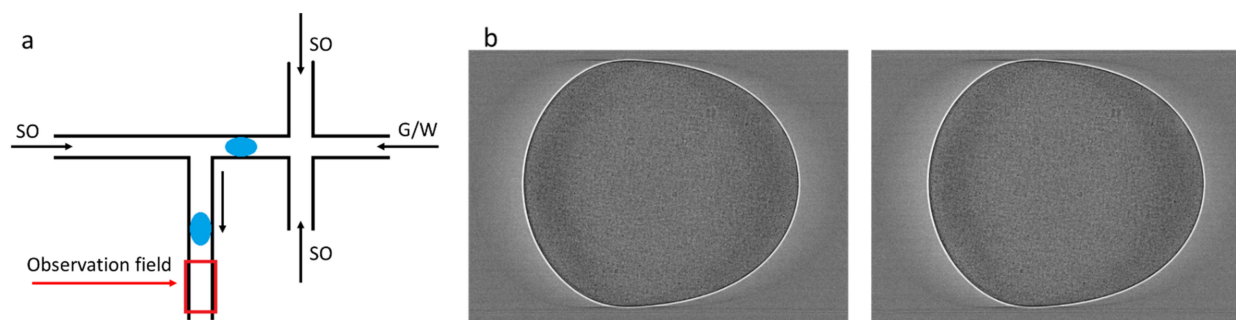


Figure 2. (a) Schematic of the microfluidic device and (b) an example of two subsequent images with speckle patterns used in PIVlab to extract velocity fields. Drops are moving from the left to the right.

The channel width was estimated from video recordings of drops moving inside the channel. To measure the channel height, several control devices were sealed with a PDMS slab of 1 mm thickness attached to a glass slide. The devices were filled with silicone oil and, after 1 week, 1 month, and 2 months, were cut from the glass, then cut in slices perpendicular to the channels and the channel depth was measured using a microscope. The changes in channel height over time were within the error for each measurement, thus, it appears that the height is less prone to changes due to swelling than channel width.

Drops were formed in the flow-focusing cross-junction. Liquids were supplied to the junction by syringe pumps (AI-4000 (World Precision Instruments)) equipped with 5 mL plastic syringes (Fisher). The length of drops was varied in the range of $W-1.4W$ for all studied compositions. The size of drops was regulated by changing the flow rate of both dispersed, Q_d , (6–13 $\mu\text{L}/\text{min}$) and continuous, Q_c , ($2 \times 2-5 \mu\text{L}/\text{min}$) phase at the cross-junction. After any change in flow rate, the flow was allowed to stabilize for at least 5 min before the measurements were started. The flow fields inside the drops were measured in the output channel after the T-junction. To make measurements under the same flow conditions, a compensating amount of continuous phase was added through an auxiliary channel at a downstream T-junction to maintain a constant flow rate in the observation channel of 32 $\mu\text{L}/\text{min}$. At this flow rate, the superficial flow velocity, $V_s = 9.2 \text{ mm}/\text{s}$, and capillary number, Ca , based on the superficial flow velocity and viscosity of continuous phase,

$$Ca = \frac{\mu_c V_s}{\sigma} = 0.013,$$

where μ_c is the viscosity of the continuous phase and σ is the interfacial tension. The Reynolds number,

$$Re = \frac{\rho_c V_s W}{\mu_c} \sim 0.06 \ll 1,$$

where ρ_c is the density of continuous phase. The volume fraction of dispersed phase, $Q_d/(Q_d + Q_c) < 0.5$; therefore, drops can be considered as hydrodynamically isolated [21].

Flow fields were measured always in the same position at a distance of $\sim 10 W$ (within the window of 3.3–3.8 mm) from the T-junction, as indicated by the red box in Figure 2a. All flow patterns inside the studied drops were completely symmetrical, confirming that this distance was large enough to eliminate all possible distortions imposed by the junction. The distance between the cross-junction, where drops were formed, and the T-junction is 5.62 mm. Considering that the superficial velocity in the channel leading to the T-junction is smaller than that in the output channel, drops reach the observation field one at a time, $t > 1$ s. This is the characteristic time for surfactant adsorption in this study.

Flow fields inside the dispersed phase were studied using Ghost Particle Velocimetry (GPV) [40–43]. This method uses the speckle patterns of white light scattered by particles smaller than the diffraction limit as flow tracers; in this study, polystyrene particles of 200 nm diameter (10% solid, Sigma Aldrich, Salisbury, UK, product number 69057) were used. The dispersion of nano-particles was diluted by the dispersed phase at a ratio of 1:50 ($v:v$). The moving drops were recorded by a high-speed video camera (Photron SA-5) connected to an inverted microscope (Nikon Eclipse Ti2-U) at 10,000 fps, with an exposure time of 0.04 ms and at $40\times$ magnification giving an image resolution of $0.5 \mu\text{m}/\text{pixel}$. The observed speckle size is defined by the light wavelength, λ , and the numerical aperture of the condenser, NA_C , $\delta_x \sim \frac{\lambda}{NA_C}$.

The resolution in the direction of the optical axis, i.e., the thickness of the layer contributing to the speckle pattern, $\delta_z \sim \frac{\lambda}{NA_C^2}$.

The mean wavelength of the microscope light source is $\lambda \sim 500$ nm, and the numerical aperture was adjusted to ~ 0.2 , resulting in $\delta_x \sim 2.5 \mu\text{m}$ and $\delta_z \sim 12.5 \mu\text{m}$. Comparison of this latter value with the channel height shows that moving the focal plane inside the drop enables the probing of the flow fields in several cross-sections over the channel height. In particular, the flow fields were recorded at the middle plane of the channel and at distances of 20, 40, 60 and $80 \mu\text{m}$ from it. The flow fields were similar for both the top and bottom parts of the channel, but the level of noise was smaller for the top part; therefore, the images from the top part were mostly used in GPV. The cross-section at $80 \mu\text{m}$ is very close to the channel wall; therefore, the layer of nanoparticles contributing to the speckle pattern was smaller. In this case, the flow field was averaged over a larger number of frames than for other cross-sections, to obtain a reliable velocity distribution. For each set of parameters, at least three drops were recorded, with at least 100 frames in each recording.

Images were pre-processed using the freeware package ImageJ [44], by subtracting the average background contribution to obtain visible speckle patterns; examples are shown in Figure 2b. The flow fields were then extracted from image sequences using PIVlab 2.36 for MATLAB [45].

3. Results and Discussion

3.1. Surfactant-Free Drops

Figure 3 shows the flow fields in a Lagrangian frame, moving with the drop, within a surfactant-free drop moving inside the channel. This was obtained by subtracting the average drop velocity from the Eulerian (stationary) GPV flow fields, which are shown in the Supplementary Materials, Figure S1. In the middle plane cross-section (Figure 3a), the velocity at the front and rear is similar to the drop velocity, leading to the respective stagnation points in the Lagrangian frame. The velocity near the side walls of the channel (top and bottom of the drop image) is smaller than the drop velocity, due to retardation from the thin film of continuous phase separating the dispersed phase from the walls. The largest velocity, $\sim 30\%$ higher than the drop velocity, is observed in the central part of the drop. Analysis of the velocity gradients around the stagnation points reveals that, at the front stagnation point, liquid moves up and down from the middle plane, whereas at the rear stagnation point, liquid moves into the middle plane from the top and bottom of the channel. The sink and source in the middle plane indicate the presence of a recirculatory flow in the drop cross-section, parallel to the side walls, with flow moving in the direction of drop motion around the middle plane and in the opposite direction near the top/bottom

wall. These will hereafter be referred to as vertical vortices. The larger velocities close to the interface in the areas indicated by arrows are due to interactions with the slugs of continuous phase separating the drops and with the corner flow.

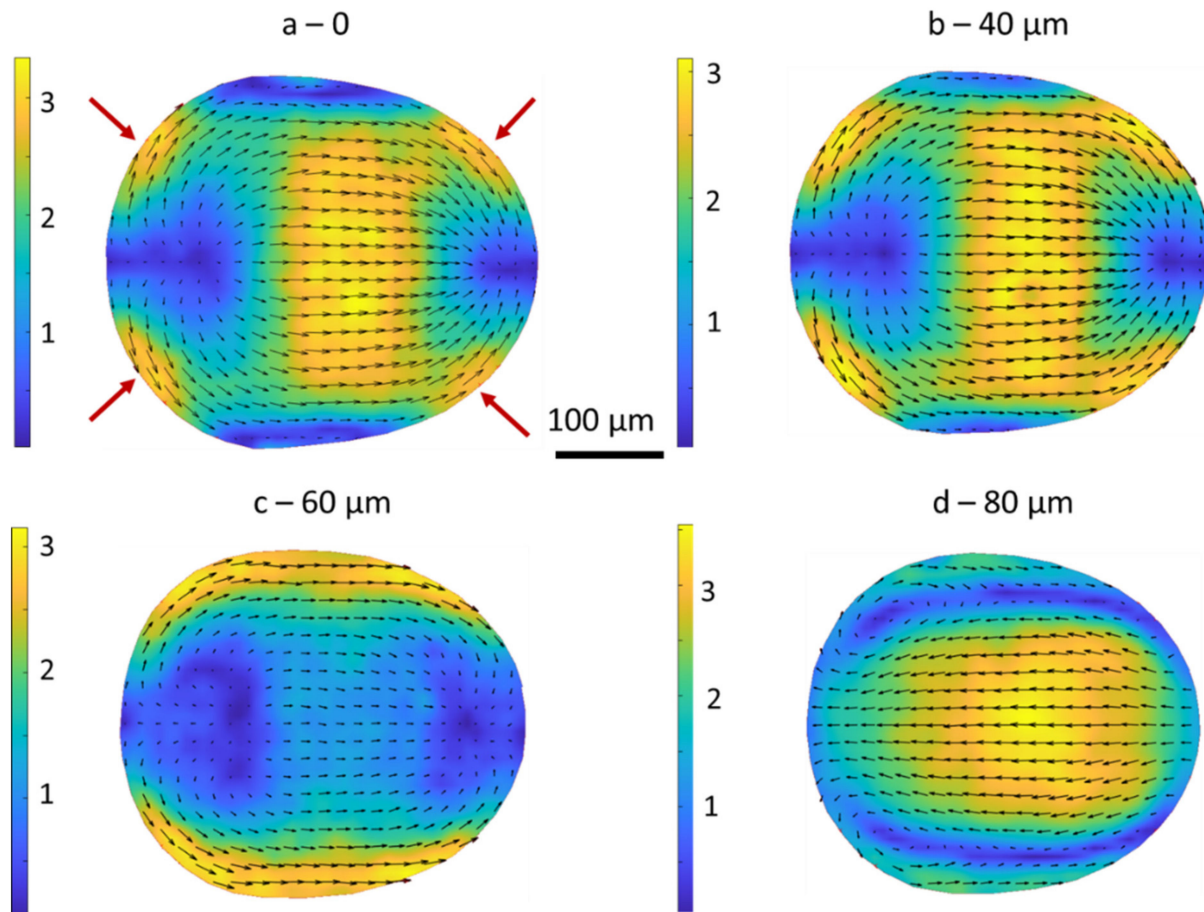


Figure 3. Flow fields inside a surfactant-free drop in the co-ordinate frame moving with the drop: (a) drop cross-section corresponding to the middle plane of the channel, (b) cross-section at 40 μm from the middle plane, (c) 60 μm , (d) 80 μm . Drop length $L = 396 \pm 3 \mu\text{m}$, drop velocity $V_d = 10.7 \pm 0.3 \text{ mm/s}$. Total flow rate $Q = 32 \mu\text{L/min}$. The velocity on color scales is given in mm/s.

Moving 20 and 40 μm from the central plane yields no noticeable change in flow pattern (Figure 3b), although the velocity difference across the drop decreases. Firstly, at a cross-section of 40 μm , the flow near the side walls reverses: the velocity here becomes slightly larger than the drop velocity, due to the larger distance to the wall and the transition of the continuous phase from film flow to the corner flow. Secondly, the velocity in the central part of the cross-section becomes smaller, because this cross-section is closer to the stagnation plane of the vertical vortices.

Measurements taken at 60 μm from the middle plane show a complete change of the flow pattern (Figure 3c), with the velocity in the inner part becoming close to the drop velocity, whereas that at the sides becomes much larger, due to drag from the continuous phase corner flow. This cross-section demonstrates the complexity of the interaction between the vertical and horizontal vortices. As the flow in the central part of this cross-section is still in the direction of the drop motion, it can be concluded that the stagnation plane for vertical vortices is closer to the top/bottom wall.

Measurements made in the cross-section close to the top/bottom wall (80 μm) show a well-developed return flow for the vertical vortices, and clear recirculation in the horizontal plane, where the liquid flowing in the direction of drop motion near the side walls returns

in the middle of the cross-section (Figure 3d). The velocity due to corner flow is smaller in this cross-section, but the difference between the minimum and maximum velocity within this plane becomes even larger than that for the middle plane.

These findings show that for a channel aspect ratio close to 0.5 and a total flow rate $Q = 32 \mu\text{L}/\text{min}$ ($Ca = 0.013$), the bulk flow field inside surfactant-free drops is formed by a pair of vertical vortices, resulting from the interaction of the pressure-driven drop motion within the channel and retardation stress from the top/bottom wall, a pair of horizontal vortices near the side walls, and two pairs of vortices caused by the accelerating action of the fast-moving continuous phase corner flow. The last vortices are expected to develop on the diagonal planes of the channel.

The intensity of the recirculation within the horizontal vortices near the side walls increases with an increase in the drop length. The vortices disappear as the drop length falls below the channel width. With this exception, the flow topology remains the same over the studied range of drop lengths. Note, this topology is accompanied by interfacial recirculatory flows: in the Lagrangian frame, the interfacial velocity near the walls is negative, whereas that in contact with the corner flow of continuous phase is positive, as shown in Figure 1. This is the essential difference between the interfacial flow accompanying the drop movement in rectangular channels from that in a cylindrical channel or an unbounded liquid, where the interfacial flow is unidirectional and acts to sweep surfactant, if present, to the rear part of the drop.

A similar 3-D flow structure was reported in [23] for a drop with $L = 2W$, moving in a channel of $100 \times 58 \mu\text{m}$ with $V_S = 0.257 \text{ mm}/\text{s}$ (Ca was not reported), whereas a more complicated flow pattern, with additional pairs of vortices at the front and rear of the drop, was observed in [25] for $L = 1.58W$, channel size $\sim 100 \times 100 \mu\text{m}$, $V_S = 5 \text{ mm}/\text{s}$, $Ca = 0.005$. The difference in the flow patterns between the present study and [25] is probably related to the difference in the channel aspect ratio and to the large difference in the viscosity ratio, μ_d/μ_c , which was 0.125 in the present study and 2.625 in [25].

Under conditions quite similar to the present study, a transition in the flow patterns in the middle plane, from one with relatively low velocity in the central part of the cross-section to one with much higher velocity, was observed in [27] at $Ca = 0.038$. Considering that the addition of surfactant in this study increases the value of the capillary number up to $Ca = 0.1$, based upon the lowest value of equilibrium interfacial tension, flow fields inside surfactant-free drops were studied additionally at flow rates of 64 and 96 $\mu\text{L}/\text{min}$ ($Ca = 0.026$ and $Ca = 0.040$), to distinguish between the effect of the lowering of the equilibrium interfacial tension and the effect of surfactant dynamics. A considerable change in flow pattern was observed already at $Ca = 0.026$. The change becomes even more pronounced at $Ca = 0.04$ (Figure 4). The flow pattern in the middle plane at $Ca = 0.04$ was similar to that observed in [27] after the transition.

An increase in the capillary number results in larger drop deformation: drop width decreased from 343 μm at $Ca = 0.013$ to 315 μm at $Ca = 0.026$, at the same drop length of 431 μm . The consequential increase in the thickness of liquid films separating the drop from the walls causes a considerable decrease in film resistance and, thus, redistribution of the continuous phase flow between films and corners. As a result, the velocity of the corner flow decreases and becomes similar to the drop velocity (Figure S2, Figure 4, top panel). The flow inside the drop at $Ca \geq 0.026$ is then dominated by two vertical vortices, and the interfacial flow is directed from the front to the rear of the drop. The diminished importance of corner flow with an increase in the capillary number is in line with theoretical predictions [18–20]. The velocity in the areas indicated by arrows in Figure 3a is still larger than the drop velocity in Figure 4, but the difference is much smaller than in Figure 3 because there is no longer a contribution from the corner flow. In the corner flow vortices, the liquid velocity is larger than the drop velocity on the surface, and smaller than the drop velocity near the drop axis, i.e., the rotation direction in the corner flow vortices is opposite to the vertical and horizontal vortices and retards them. That is why the disappearance of corner flow vortices causes a larger velocity in the central part of the drop.

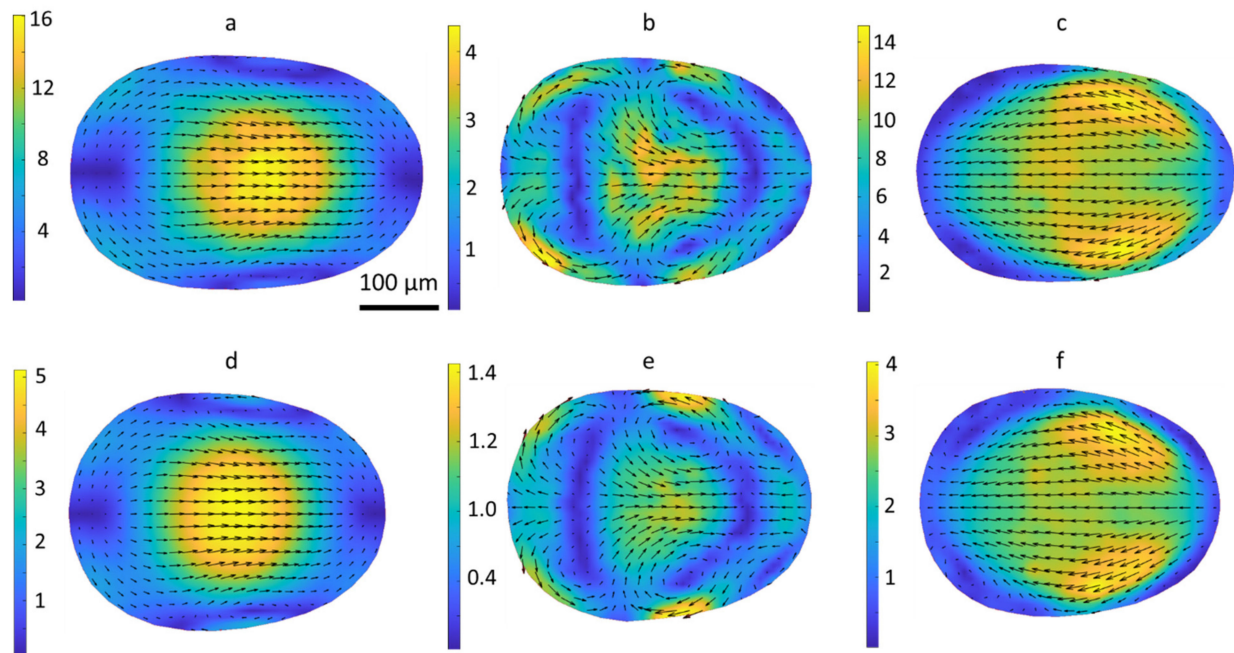


Figure 4. Flow fields inside a drop in the co-ordinate frame of the drop: top panel, surfactant-free, total flow rate $Q = 96 \mu\text{L}/\text{min}$, $Ca = 0.040$, drop length $L = 430 \pm 20 \mu\text{m}$, drop velocity $V_d = 34.1 \pm 0.8 \text{ mm}/\text{s}$, (a)—middle plane, (b)—60 μm from the middle plane, (c)—80 μm ; bottom panel, $C_{10}\text{TAB}$, 1.5 cmc, $Q = 32 \mu\text{L}/\text{min}$, $Ca = 0.037$, drop length $L = 397 \pm 6 \mu\text{m}$, drop velocity $V_d = 11.1 \pm 0.3 \text{ mm}/\text{s}$, (d)—middle plane, (e)—60 μm from the middle plane, (f)—80 μm . The velocity on color scales is given in mm/s .

3.2. Surfactant Properties

The dependence of interfacial tension between the aqueous phase and silicone oil on the surfactant concentration is presented in Figure 5. The data were fitted to the Szyszkowski–Langmuir equation of state:

$$\sigma = \sigma_0 - RT\Gamma_{\infty} \ln(1 + bc) \quad (1)$$

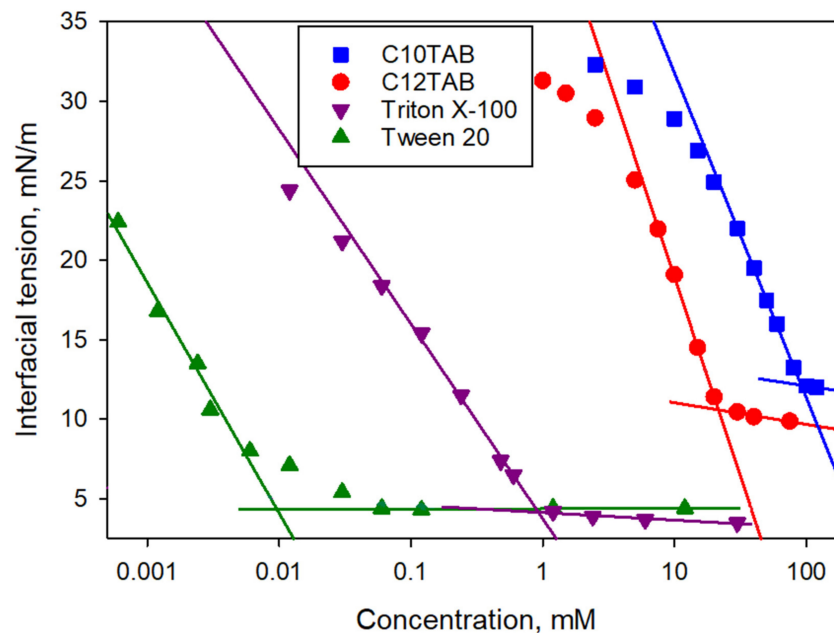


Figure 5. Concentration dependence of interfacial tension between solutions of surfactants in the glycerol/water mixture and the silicone oil.

This is directly related to the Langmuir adsorption isotherm:

$$\Gamma = \Gamma_{\infty} \frac{bc}{1 + bc} \quad (2)$$

where σ is the equilibrium interfacial tension at a bulk concentration of the surfactant c , σ_0 is the interfacial tension of a surfactant-free system, R is the universal gas constant, T is the absolute temperature, Γ_{∞} is the maximum adsorption, Γ is the equilibrium adsorption at concentration c , and b is the adsorption constant. The parameters of Equations (1) and (2), Γ_{∞} and b , together with the values of critical micelle concentration (CMC) and interfacial tension at CMC found in Figure 5, are collected in Table 2. The CMC values for ionic surfactants in the water/glycerol mixture are larger than for solutions in water [46], which is in line with other studies [47,48]. CMC for Triton X-100 is also larger than data from the literature [46] and from the supplier for solutions in water, 0.6 mM.

Table 2. Properties of surfactants used.

Surfactant	CMC, mol/m ³	σ at CMC, mN/m	Γ_{∞} , mol/m ²	b , m ³ /mol	h_D at CMC, μ m	D , m ² /s	t_D at CMC, ms
C ₁₀ TAB	90	12.1	$5.7 \cdot 10^{-6}$	$4.46 \cdot 10^{-2}$	0.063	$1 \cdot 10^{-10}$	0.04
C ₁₂ TAB	21	10.4	$8.0 \cdot 10^{-6}$	$1.085 \cdot 10^{-1}$	0.38	$9 \cdot 10^{-11}$	1.6
Triton X-100	0.95	4.2	$2.0 \cdot 10^{-6}$	$3.66 \cdot 10^2$	2.1	$6 \cdot 10^{-11}$	74
Tween 20	0.01–0.06	4.4	$3.1 \cdot 10^{-6}$	$5.66 \cdot 10^3$	310–52	$4 \cdot 10^{-11}$	$(2.4-0.07) \cdot 10^6$

A range of concentration values for the CMC of Tween 20 is given in Table 2 because the rate of change of interfacial tension with concentration reduces markedly at concentrations above 0.01 mM and then flattens off at 0.06 mM. Tween 20 can contain a mixture of homologs with various numbers of ethylene oxide units, with the average number being 20. It can be assumed that various homologs begin to form micelles at different concentrations, and this is the reason that the slope reduces over a concentration range. A similar change in the slope of $\sigma(c)$ was found in [49] at the interface of aqueous solution with toluene, whereas it was absent at the interface with air. Moreover, it was found in [49] that the CMC decreases if the aqueous phase is in contact with toluene. This decrease was ascribed to toluene dissolution in water. Considering that glycerol is less polar than water, the presence of glycerol can result in a decrease in CMC for Tween 20. The CMC value of 0.06 mM is in line with the values for water provided by the supplier and found in the literature (see [49] and references therein). Obviously, the part of the curve above 0.01 mM cannot be described by Equation (1). Therefore, the isotherm parameters for Tween 20 in Table 2 are valid only for concentrations ≤ 0.01 mM, although in what follows, 0.06 mM is accepted as the value of CMC.

Considering the dynamic character of the moving drop interface, as well as the short timescales of microfluidic processes, the characteristic timescale of surfactant adsorption is an important parameter for this study. Comparison of the adsorption timescale with drop age at the observation point (1 s) shows whether the equilibrium interfacial tension has been reached. Comparison with the characteristic timescale of drop surface deformation will show whether additional dynamic effects can be expected. The timescale of drop surface deformation can be estimated from the gradients of surface velocity. Figure 3 shows that the velocity changes along the surface are of the order of 3 mm/s and occur at the length scale $L/2-L/4$. This gives the timescale of surface deformation as being around 20–30 ms.

Diffusion-controlled adsorption kinetics are assumed here as typical for non-polymeric surfactants. It was found in [50] that the kinetics of CnTAB surfactants can be described reasonably well by a diffusion model, using the Frumkin isotherm. The best agreement between theory and experiment for the kinetics of surfactant adsorption at the water/air interface was found for an isotherm accounting for compressibility of the surfactant adsorp-

tion layer. Fitting data in Figure 5, using the Frumkin compressibility model, shows that for the aqueous/silicone oil interface, the best fit corresponds to the Frumkin interaction parameter equal to zero for both ionic surfactants (i.e., the Langmuir model) with compressibility $\varepsilon = 0$ for C₁₂TAB and $\varepsilon = 0.001$ for C₁₀TAB. The difference in the values of isotherm parameters for the simple Langmuir model, Equations (1) and (2), and the compressibility model is within 3% and, thus, can be neglected. Diffusion-controlled kinetics was successfully used in [49] to describe the dynamic surface and interfacial tension of Tween 20. For Triton X-100, adsorption kinetics at the water/air interface can be described as diffusion-controlled if a more sophisticated adsorption isotherm accounting for molecular reorientation at the interface is used; however, acceptable results were obtained with the Frumkin model [51]. Fitting data in Figure 5 with the Frumkin model gives an interaction parameter of -0.4 , and the value of Γ_∞ is only 4% larger than that presented in Table 2. Therefore, using diffusion-limited adsorption kinetics is justified also for Triton X-100. The characteristic length scale for adsorption, h_D , can be estimated as a thickness of a solution layer containing the number of molecules necessary to form an adsorption layer [52]:

$$h_D = \frac{\Gamma}{c} \quad (3)$$

The characteristic diffusion time scale, t_D , can be estimated as:

$$t_D = \frac{h_D^2}{D} = \frac{\Gamma^2}{Dc^2} \quad (4)$$

where D is the diffusion coefficient.

Diffusion coefficients of the surfactant monomers in the water/glycerol mixture were calculated using the Wilke–Chang correlation [53,54] for individual liquids (water and glycerol) as:

$$D_{AB} = \frac{7.4 \times 10^{-8} (\phi M_B)^{1/2} T}{\mu_B V_A^{0.6}} \quad (5)$$

where D_{AB} is the diffusion coefficient of solute A in solvent B in cm^2/s , M_B is the molecular mass of solvent in mol/cm^3 , μ_B is the viscosity of solvent in $\text{cP} = \text{mPa}\cdot\text{s}$, V_A is the molar volume of solute at its normal boiling temperature in cm^3/mol , ϕ is the association factor of the solvent, with 2.6 for water and 1, non-associated solvents. V_A was estimated using the Le Bas method [53,54].

The diffusion in water/glycerol mixture was calculated as [55]:

$$D_{AG-W} = \frac{X_W D_{AW} \mu_W^{0.8} + X_G D_{AG} \mu_G^{0.8}}{\mu_{G-W}^{0.8}} \quad (6)$$

where X is the molar fraction of a component in a mixture, and subscripts W , G and G_W mean water, glycerol and glycerol/water mixture.

At concentrations above the CMC, micelles provide an additional contribution to surfactant mass transfer. In this case, an apparent diffusion coefficient, D^* , can be calculated as [56]:

$$D^* = D(1 + \beta) \left(1 + \beta n^{-1/3}\right) \quad (7)$$

where $\beta = (c - \text{CMC})/\text{CMC}$ and n is the micelle aggregation number.

Characteristic diffusion lengths and timescales for the surfactants used in this study, at a concentration equal to the CMC, are presented in Table 2. The validity of calculated timescales is supported by Figure 6, where the dynamic surface tension (aqueous phase/air) is presented for surfactant solutions at the CMC in the glycerol/water mixture (a concentration of 0.06 mM was taken for Tween 20). The characteristic timescale of adsorption should be rather similar for both aqueous/air and aqueous/SO interfaces, because the surfactant diffusion coefficient and concentration (CMC) included in Equation (4) are the same, and

the values of maximum adsorption presented in Table 1 are quite close to those for an air/water interface (see, for example, [46]). Figure 6 shows a very short adsorption time for both ionic surfactants, with equilibration time being below the timescale of measurement. For TX-100, Figure 6 shows an equilibration time below 1 s, whereas for Tween 20 it is much larger than the time of measurement. At a timescale of 10 s, the surface tension is only slightly smaller than the surface tension of a surfactant-free glycerol/water mixture.

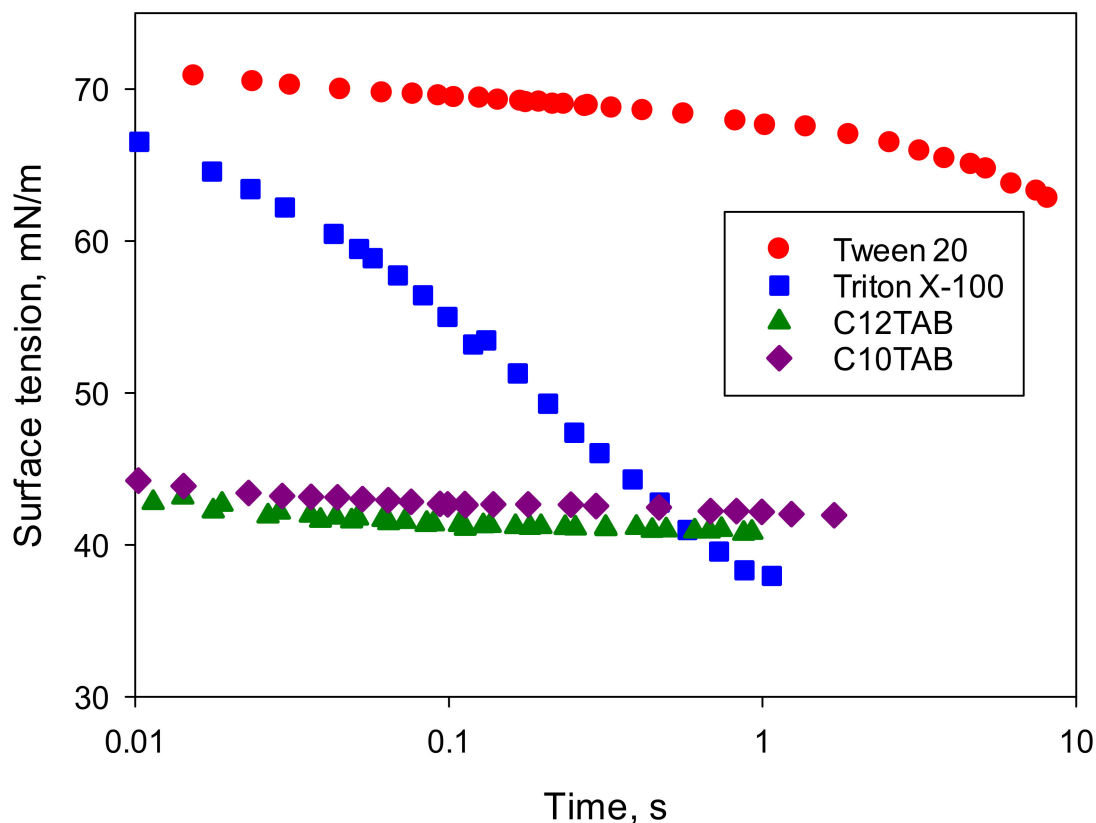


Figure 6. Dynamic surface tension of surfactant solutions in the glycerol/water mixture at concentrations equal to CMC values. A concentration of 0.06 mM is used for Tween 20. For C₁₀TAB and C₁₂TAB, the equilibrium surface tension was reached at $t < 0.01$ s, for Triton X100 it was reached at $t \sim 1$ s; for Tween 20, surface tension was far from equilibrium at $t = 10$ s.

For ionic surfactants with high values of CMC, the characteristic length of scales are much smaller than the drop size, and the characteristic timescale is much smaller than both the drop age at observation and the characteristic time of surface deformation. Therefore, for those two surfactants, no dynamic effects are expected. Moreover, the convection within the drop will hardly accelerate the adsorption kinetics.

For Triton X-100, the characteristic adsorption timescale is slightly smaller than the observation time, but longer than the characteristic time of surface deformation; therefore, interfacial tension should be close to the equilibrium interfacial tension at the time of observation, but one can expect dynamic effects related to the surface deformation. Due to complicated flow patterns inside the drop, it is difficult to estimate the characteristic length of the diffusion boundary layer and corresponding characteristic diffusion time. A very rough estimation, based on [57], gives the value of an order of $L/V_d \sim 40$ ms. This time is of the same order of magnitude as the adsorption time of diffusion-controlled kinetics. Therefore, for Triton X-100, convective mass transfer contributes to the total mass transfer, although it should have no significant importance.

For Tween 20, the characteristic adsorption timescale is very large (around 70 s for concentration 0.06 mM and around 40 min for a concentration of 0.01 mM) and the char-

characteristic adsorption length is comparable to the drop size. This affects both equilibrium and dynamic surface tension. First of all, the convection within the drop of Tween 20 solution should be important for adsorption acceleration because the convection removes depleted solution adjacent to the interface and replaces it with a surfactant-rich solution from the drop bulk. The characteristic time related to the diffusion boundary layer is noticeably smaller than the drop age at the observation point; therefore, even for this slowly equilibrating surfactant, drops are expected to reach the equilibrium interfacial tension at the observation point. However, this time is of the same order of magnitude as the drop deformation time and, thus, the dynamic effects related to surface deformation can be observed.

As the diffusion length scale for Tween 20 is close to the drop size, a substantial depletion of the surfactant from the bulk due to adsorption is expected. At equilibrium, surfactant mass balance can be written as:

$$c = c_0 - \frac{S}{V}\Gamma \quad (8)$$

where c is the surfactant concentration after adsorption is completed, c_0 is the initial surfactant concentration, S is the drop surface area, V is the drop volume and Γ is the equilibrium adsorption value. The smaller the drop size, the larger the area/volume ratio and, thus, the larger the proportion of surfactant transferred from the bulk to the interface. At $c = \text{CMC}$, $\Gamma \sim \Gamma_\infty$. It is easy to estimate that for a drop of 350 μm size in the plane of observation laden with Tween 20 ($\Gamma_\infty \sim 3.1 \times 10^{-6} \text{ mol/m}^2$) at concentrations above CMC $c_0 - c \sim 0.07 \text{ mM}$, which is larger than the CMC value. To get a surface concentration close to Γ_∞ , the initial concentration of Tween 20 in the dispersed phase should be at least 0.08 mM. Therefore, the depletion of surfactants from the bulk phase due to adsorption is essential and should be always taken into account. This effect becomes smaller with an increase in CMC value. It is still noticeable for TX-100, but it can be neglected for ionic surfactants with $\text{CMC} > 1 \text{ mM}$.

There is, however, another source of depletion for ionic surfactants. According to the supplier (Sigma Aldrich), the nanoparticles used in this study are carboxylate-modified, i.e., their surface is negatively charged, due to the presence of free carboxy groups. It is, therefore, expected that the cationic surfactants used in this study, C_{10}TAB and C_{12}TAB , will adsorb onto the surface of the nano-particles due to electrostatic attraction. If the same adsorption density for the liquid/liquid and liquid/solid interface is assumed, there can be a depletion of surfactant from the bulk up to 1 mM at CMC; this is less than 5% of surfactant for C_{12}TAB and slightly more than 1% for C_{10}TAB and, thus, such depletion can be neglected.

3.3. Surfactant-Laden Drops

The addition of a surfactant with a large CMC value and a short equilibration time, such as C_{10}TAB and C_{12}TAB , changes the flow pattern in a similar way to that observed with an increase in flow rate. As the surfactant concentration increases and the interfacial tension decreases, the drop deforms more. There is a consequent increase in the thickness of the continuous phase liquid film between the drop and the wall and thus the corner flow slows down. Transition to the flow pattern dominated by two vertical vortices was observed above the critical capillary number. The similarity of flow patterns between the surfactant-laden and surfactant-free cases, at similar values of capillary number, is clear from a comparison of the top and bottom panels in Figure 4.

The transition in the flow patterns is accompanied by a change of the drop shape from bullet-like, with a large difference in curvatures between the front and rear of the drop, to nearly symmetrical (compare Figures 3 and 4, see Figure S3 for comparison with C_{10}TAB -laden drops of 80 mM and 120 mM) and a noticeable, $\sim 10\%$, increase in the drop velocity.

In the absence of corner flow, the interface stretches at the front of the drops and contracts at the rear of the drop, i.e., the surfactant is being swept to the rear part of the drop. However, for C_{10} TAB and C_{12} TAB surfactants, the equilibration time (0.01 and 0.9 ms, respectively) is much shorter than the characteristic time of surface deformation (~ 20 ms). Therefore, for these surfactants, the effect of surface deformation is negligible and minimal depletion of surfactant from the interface would be expected.

There is an important effect of surfactant concentration on the relative velocity differences within the horizontal cross-section of the drop. Figure 7 presents the dependence of the difference between the maximum and minimum velocity in the middle plane (taken in the Eulerian frame) normalized by drop velocity, on the drop size normalized by channel width. As expected, the velocity difference increases with an increase in the drop length, because of the stronger effect of the channel wall. As shown in Figure 8, an increase in the drop length results in a decrease in minimum velocity in the middle cross-section, which is the velocity near the wall, but it also results in an increase in maximum velocity, meaning an increased recirculation in vertical vortices. For the same reason, the difference decreases with an increase in surfactant concentration: the drop becomes more deformable and, at the same length, the drop width and the retarding effect of the continuous phase film become smaller, i.e., the minimum velocity in the middle cross-section increases considerably (Figure 8). There is also some increase in the maximum velocity, which can be ascribed to the decreased intensity of recirculation in the corner flow vortices and, thus, its retarding effect of vertical vortices.

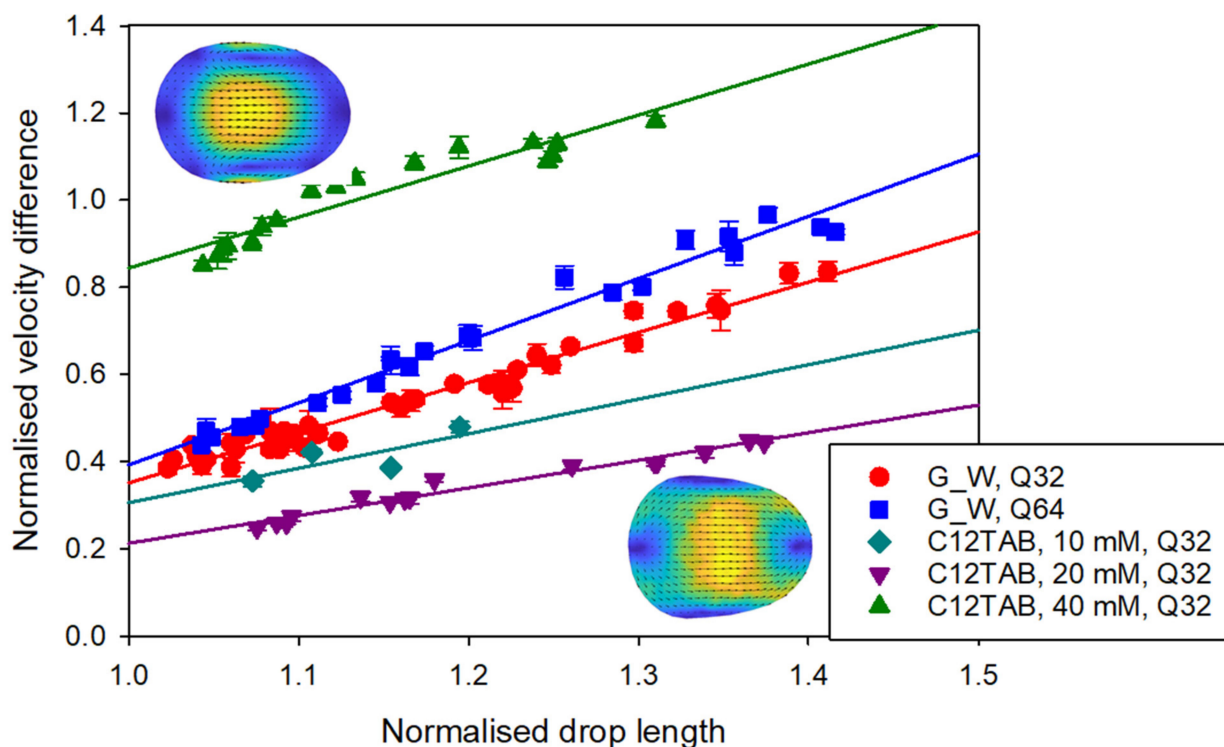


Figure 7. Dependence of normalized velocity difference in the middle plane on normalized drop length for surfactant-free dispersed phase and various concentrations of C_{12} TAB. Q32 corresponds to the total flow rate $Q = 32 \mu\text{L}/\text{min}$, and Q64 corresponds to the total flow rate $Q = 64 \mu\text{L}/\text{min}$.

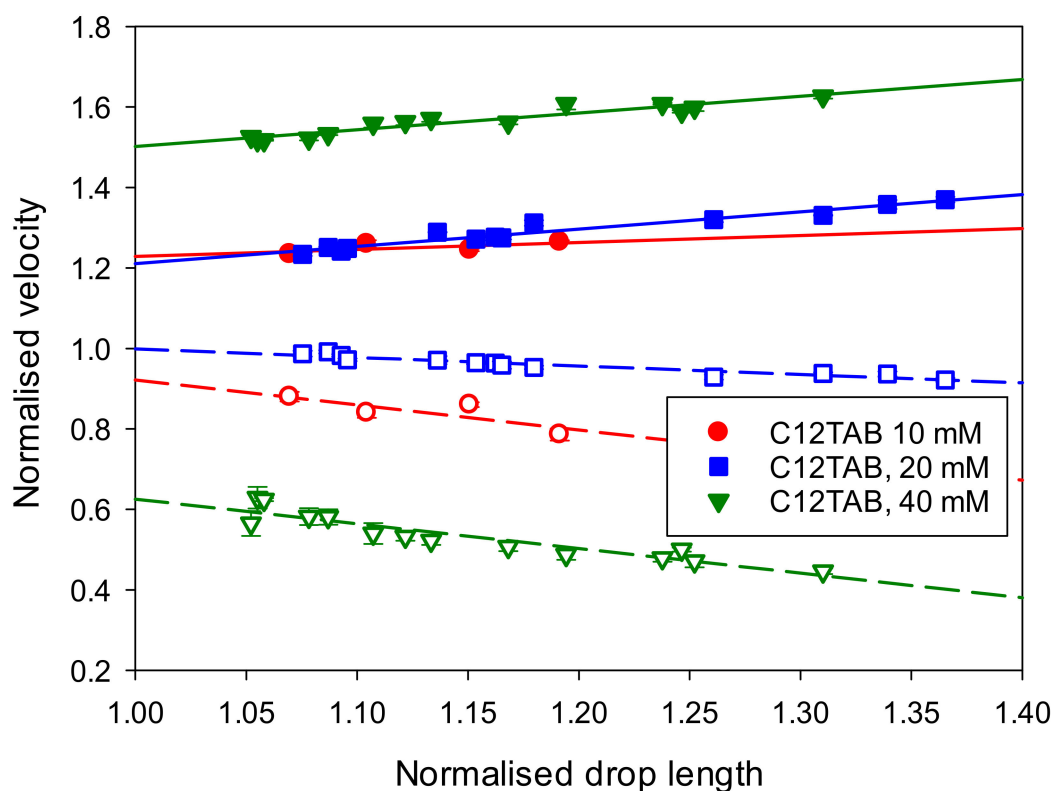


Figure 8. Dependence on the minimum and maximum velocity in the middle drop cross-section, normalized by the drop velocity on the drop length, normalized by the channel width for various concentrations of $C_{12}TAB$. Filled symbols are for maximum velocity and empty symbols are for minimum velocity.

At further increases in concentration, after a transition to the regime without corner flow, the velocity difference grows sharply, and for large drops, it exceeds the drop velocity (Figure 7). Thus, the addition of a fast-equilibrating surfactant can considerably increase the shear stresses inside the drop. The sharp increase in the velocity difference is caused by a further increase in the maximum velocity, but also by a considerable decrease in the minimum velocity (Figure 8). This might be thought of as counterintuitive, but can be explained by considering the interaction between surface flow in the corners and the horizontal vortices. Due to the channel aspect ratio, the area of the drop in contact with side wall films is small and, thus, corner flow has a noticeable accelerating effect on the velocity of the film. After transition to the regime with negligible corner flow, this acceleration disappears and the flow in the films becomes slower.

The addition of a surfactant with a slower equilibration rate, such as Triton X-100, also results in a change of flow patterns within a drop, but as is shown in Figure 9, this change is very different from that which was previously observed for $C_{10}TAB$ and $C_{12}TAB$. In this case, the corner flow becomes increasingly important, and flow in the middle of the drop is reversed, so the recirculation patterns related to the corner flow are clearly visible in each cross-section. The concentration at transition is far below the CMC for Triton X-100; the drop has the bullet shape with a larger curvature at the front, and smaller at the rear of the drop, and the drop velocity is similar or even a little smaller than that for a surfactant-free-drop.

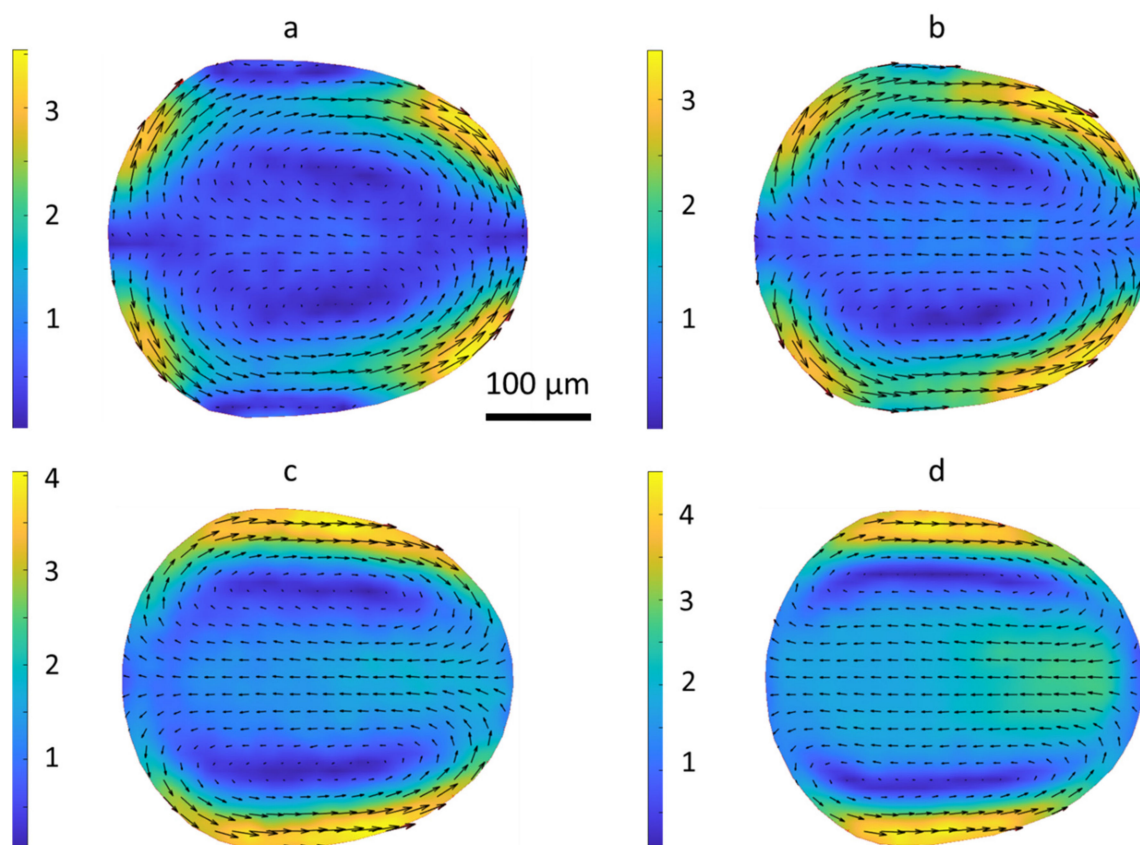


Figure 9. Flow patterns within the drop laden with Triton X-100, at a concentration of 0.3 mM \sim 0.3 CMC. Drop length $L = 392 \mu\text{m}$, total follow rate $Q = 32 \mu\text{L}/\text{min}$, drop velocity $V_d = 9.6 \text{ mm}/\text{s}$, (a)—middle plane, (b)—40 μm from the middle plane, (c)—60 μm , (d)—80 μm .

A similar transition was observed for Tween 20. As shown in Figure 10, with an increase in surfactant concentration, the flow velocity in the central part of the middle plane decreases, due to the growing retarding effect of the corner flow, and flow reversal occurs at a concentration of 3 CMC = 0.18 mM. The flow patterns remain unchanged for a further concentration increase from 3 to 30 CMC. Unlike the flow in the central part, the symmetrical areas of large flow velocity at the front and rear parts of the drop, which are related to the interaction of the drop flow field with the continuous phase (mostly the corner flow (compare Figures 4, 9 and 10)), remain in place with an increase in concentration. The flow distribution in the various cross-sections is similar for Triton X-100- and Tween 20-laden drops, as illustrated by a comparison of Figure 9 and Figure S4.

To verify that the flow patterns depend on dynamic effects related to the surfactant redistribution, rather than on interfacial tension at the time of drop observation, the velocity fields in two similar drops, laden with Tween 20 and $C_{12}\text{TAB}$, were compared. The chosen drops have the same length, $L = 368 \mu\text{m}$, are moving with the same velocity, $V_d = 9.8 \text{ mm}/\text{s}$; moreover, they have the same shape in the middle plane of observation, as shown in Figure 11a. This suggests that the interfacial tension is the same for the two drops, i.e., the interfacial tension for the Tween-laden drop is $\geq 19.1 \text{ mN}/\text{m}$, considerably higher than the equilibrium interfacial tension at this concentration (even accounting for surfactant depletion from the bulk). This agrees with the high value of characteristic diffusional adsorption time given in Table 2 and shows that, probably, the thickness of the adsorption layer inside the drop was underestimated, or that adsorption kinetics are not purely due to diffusion. Despite the similar (dynamic) interfacial tension, the flow patterns inside the two drops are very different (compare Figure 11b,c); thus, the changes in flow fields observed inside Tween 20-laden drops are due to dynamic effects caused by surfactant

redistribution. As patterns within Tween 20- and Triton X-100-laden drops are similar, we assume that dynamic effects are also of importance for the Triton X-100-laden drops.

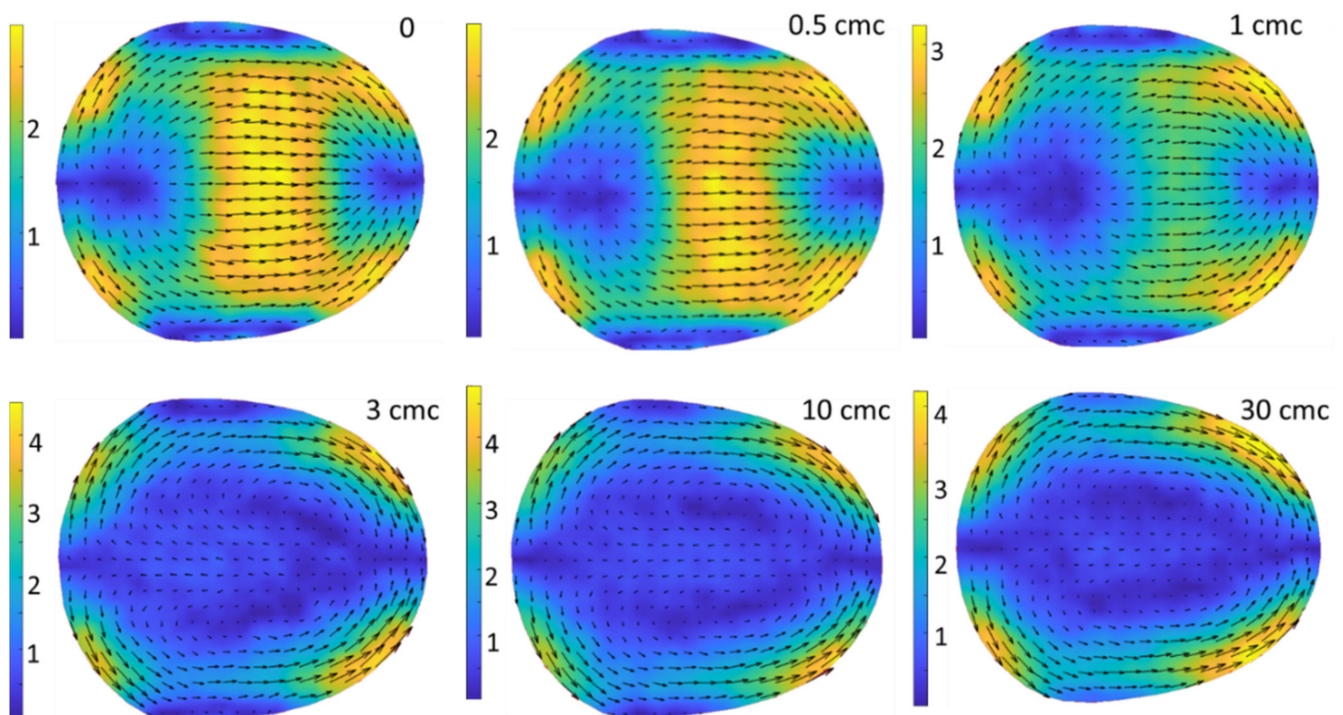


Figure 10. Flow patterns in the middle plane of a drop moving inside the channel depending on Tween 20 concentration in the coordinate system moving with the drop. Surfactant concentration is shown at each panel. Velocity on the color bar is given in mm/s. Drop velocities $V_d = 10.1 \pm 0.3$ mm/s, drop lengths $L = 384 \pm 3$ μm .

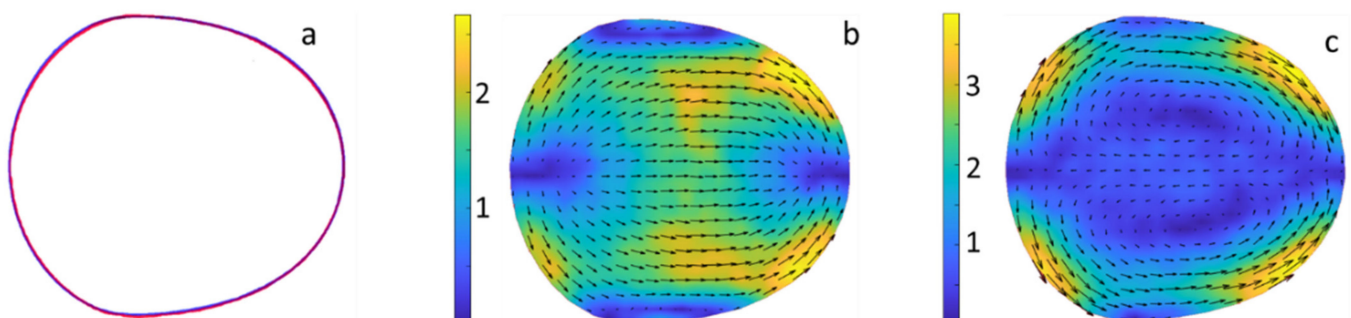


Figure 11. Comparison of C_{12} TAB- and Tween-laden drops: (a) contours of drops, blue C_{12} TAB, 10 mM (0.5 CMC); red Tween 20, 0.6 mM (10 CMC); (b) flow field in the middle plane of C_{12} TAB drop; (c) flow field in the middle plane of Tween 20 drop. Drop length $L = 368$ μm , drop velocity $V_d = 9.8$ mm/s.

As was mentioned earlier (see Figure 1), the interfacial flow near the walls is directed towards the rear of the drop, resulting in interface expansion at the front and contraction at the rear. The corner flow is oppositely directed and causes contraction at the front and expansion at the rear. Considering (see Figure 3) that the absolute values of the flow near the walls is larger than the corner flow and applies over the larger part of the perimeter of the surface element in the frontal part of the drop, it is a plausible assumption that the interface expands at the frontal part of the drop and contracts at the rear part of the drop, even in the presence of the corner flow. This results in the interfacial tension being larger at the front and smaller at the rear, facilitating the corner flow and suppressing the flow near the walls. For a slowly equilibrating surfactant, the gradient cannot be eliminated by

surfactant adsorption from the bulk and, thus, a flow pattern with a dominant corner flow is observed.

These results are in line with previous numerical simulations on surfactant-laden drops moving in a square channel [33], although the values of the Peclet number, $Pe = HV_S/D$, that were given were much smaller than in the present study. According to [33], gradients of interfacial tension over the drop surface greatly depend on the Damkohler number, $Da = \Gamma_\infty/Hc$, and become negligible at $Da < 0.01$. Γ_∞ is of the same order of magnitude for low molecular mass surfactants, including those used in this study (Table 2), whereas the concentrations providing noticeable changes of interfacial tension vary over several orders of magnitude. At CMC, for $C_{10}TAB$ and $C_{12}TAB$, $Da \sim 10^{-3}$ and, thus, dynamic effects due to surfactant redistribution are negligible, whereas these effects become significant for Triton X100 ($Da \sim 0.013$) and especially for Tween 20 ($Da \sim 0.3$). As the Damkohler number decreases with an increase in surfactant concentration, the transition to flow patterns, as presented in Figure 4, can be expected at large enough concentrations of slowly equilibrating surfactants. Such concentrations were not achieved in this study, due to wetting problems on the channel walls.

Flow patterns similar to those presented in Figure 9 and in the bottom panel of Figure 10 were observed in the presence of 1 wt % Span 80 in continuous phase at $Ca = 5.1 \cdot 10^{-2}$ [27]. At larger capillary numbers, the surfactant-laden flow field in the middle plane, as reported in [27], was similar to that in Figure 4. It was found in [28], where the surfactant Span 80 was present in the continuous phase at concentrations smaller than in [27] (0.15–0.25 wt %) that the flow in the middle plane of the drop is directed from the front to the rear in the central part (similar to Figures 9 and 10) and from the rear to the front near the walls. Note, the opposite direction was reported in other studies on surfactant-free [22,23,25–27] and surfactant-laden [22] flows. Considering that Span 80 is a slowly equilibrating surfactant, it can be assumed that the presence of slowly equilibrated surfactant in the continuous phase has a similar effect on flow patterns inside the drop, as when the surfactant is present in the dispersed phase. It could be the case that, at concentrations of 0.15–0.25%, the accelerating effect of the Marangoni stresses is large enough to overcome the wall resistance and force the liquid near the wall to flow in the direction of drop movement, but this problem requires further comprehensive study.

4. Conclusions

Flow patterns inside surfactant-free and surfactant-laden drops, moving in a rectangular microfluidic channel with an aspect ratio of 0.48, were studied using ghost particle velocimetry over a range of capillary numbers from 0.01–0.1. The viscosity ratio between the dispersed and continuous phase was fixed at 0.12. Four different surfactants, covering the CMC values 0.06–90 mM, were studied over a range of concentrations, from 0.1 to 10 CMC. Drop length varied in the range of 1–1.4 of the channel width.

Interfacial tension between surfactant solutions in a 52% glycerol/48% water mixture (dispersed phase) and silicone oil, used as the continuous phase, was measured to determine the values of CMC and parameters of Langmuir adsorption isotherm for all studied surfactants. The characteristic adsorption time for these surfactants was calculated and compared with the characteristic time of drop deformation.

For surfactant-free drops, flow patterns at $Ca = 0.013$ consisted of two symmetrical vortices near the side walls, two larger vertical vortices, due to interactions with the top/bottom wall of the channel, and four symmetrical vortices, due to corner flows. At $Ca = 0.04$, the corner flows were suppressed by larger drop deformation and a decrease in the difference in hydrodynamic resistance between the films and corners. The flow pattern, in this case, was dominated by the vertical vortices.

For surfactants with an equilibration rate considerably faster than the characteristic time of surface deformation, $C_{10}TAB$ and $C_{12}TAB$, no dynamic effects were observed and the change in flow pattern was governed by the change of capillary number, due to a change of equilibrium interfacial tension. The flow pattern at $Ca = 0.04$ was the same,

independent of whether the change in capillary number was due to a change in velocity or in interfacial tension.

For drops containing slowly equilibrated surfactants, Triton X-100 and Tween 20, transition to flow pattern dominated by corner flow was observed as the surfactant concentration was increased. Flow-mediated surface deformation should in this case lead to non-uniform surfactant distribution and Marangoni stresses accelerating the corner flow. The transition was observed at a much smaller concentration (in terms of CMC) for Triton X-100 than for Tween 20.

The analysis of flow patterns in this study is based on a comparison of the timescale of deformation of the drop surface and the timescale of surfactant adsorption, based on diffusion-limited adsorption kinetics. Such a comparison is rather approximate, but it provides a simple criterion for the effect of surfactant on flow patterns in rectangular channels: if the characteristic time of surfactant adsorption at CMC is much smaller than the characteristic time of deformation, surfactant presence suppresses the effect of corner flow; in the opposite case, the surfactant amplifies the effect of the corner flow. The characteristic timescale of surface deformation can be very roughly estimated as $L/4V_d$. For a deeper understanding of the surfactant effect and a more precise criterion, the effect of convection inside the drop on surfactant redistribution should be considered in more detail, which is possible only within high fidelity numerical simulations. Such simulations, offering scope for future work, can also account not only for purely diffusion-limited, but also mixed adsorption kinetics, in particular those related to the electrostatic barrier for the adsorption of ionic surfactants.

Supplementary Materials: The following are available online at <https://www.mdpi.com/article/10.3390/colloids5030040/s1>, Figure S1: Flow fields inside a surfactant-free drop in the co-ordinate frame of channel: (a) drop cross-section corresponding to the middle plane of channel, (b) cross-section at 40 μm from the middle plane, c –60 μm , d –80 μm . Drop length $L = 396 \pm 3 \mu\text{m}$, drop velocity $V_d = 10.7 \pm 0.3 \text{ mm/s}$. The velocity on color scales is given in mm/s, Figure S2: Flow fields inside a surfactant-free drop in the co-ordinate frame of drop. Total flow rate $Q = 64 \mu\text{L/min}$. Drop length $L = 434 \pm 5 \mu\text{m}$, drop velocity $V_d = 21.9 \pm 0.5 \text{ mm/s}$. The velocity on color scales is given in mm/s, Figure S3: Comparison of flow patterns inside the drops laden by $C_{10}\text{TAB}$: top panel $c = 80 \text{ mM}$, $L_d = 391 \mu\text{m}$, $V_d = 10.6 \text{ mm/s}$; bottom panel $c = 120 \text{ mM}$, $L = 387 \mu\text{m}$, $V_d = 11.4 \text{ mm/s}$. The velocity on color scales is given in mm/s, Figure S4: Flow fields in various cross-sections of 10 cmc (0.6 mM) Tween 20 drop, $L = 372 \mu\text{m}$, $V_d = 9.7 \text{ mm/s}$. The velocity on color scales is given in mm/s.

Author Contributions: Conceptualization, N.M.K. and M.J.H.S.; methodology, N.M.K.; investigation, N.M.K.; resources, M.J.H.S.; writing—original draft preparation, N.M.K.; writing—review and editing, M.J.H.S.; visualization, N.M.K.; funding acquisition, M.J.H.S. All authors have read and agreed to the published version of the manuscript.

Funding: This research was funded by the Engineering and Physical Sciences Research Council, UK, through the PREMIERE Programme Grant EP/T000414/1.

Institutional Review Board Statement: Not applicable.

Informed Consent Statement: Not applicable.

Conflicts of Interest: The authors declare no conflict of interest. The funders had no role in the design of the study; in the collection, analyses, or interpretation of data; in the writing of the manuscript, or in the decision to publish the result.

References

1. Dressler, O.J.; Casadevall, I.S.X.; de Mello, A.J. Chemical and Biological Dynamics Using Droplet-Based Microfluidics. *Annu. Rev. Anal. Chem.* **2017**, *10*, 1–24. [[CrossRef](#)]
2. Jankowski, P.; Samborski, A.; Ostaszewski, R.; Garstecki, P. Evaluation of droplet-based microfluidic platforms as a convenient tool for lipases and esterases assays. *Prep. Biochem. Biotechnol.* **2019**, *49*, 727–734. [[CrossRef](#)]
3. Srisa-Art, M.; Dyson, E.C.; de Mello, A.J.; Edel, J.B. Monitoring of Real-Time Streptavidin-Biotin Binding Kinetics Using Droplet Microfluidics. *Anal. Chem.* **2008**, *80*, 7063–7067. [[CrossRef](#)] [[PubMed](#)]

4. Hess, D.; Yang, T.; Stavrakis, S. Droplet-based optofluidic systems for measuring enzyme kinetics. *Anal. Bioanal. Chem.* **2020**, *412*, 3265–3283. [[CrossRef](#)] [[PubMed](#)]
5. Lombardi, D.; Dittrich, P.S. Droplet microfluidics with magnetic beads: A new tool to investigate drug-protein interactions. *Anal. Bioanal. Chem.* **2011**, *399*, 347–352. [[CrossRef](#)] [[PubMed](#)]
6. Kaushik, A.M.; Hsieh, K.; Mach, K.E.; Lewis, S.; Puleo, C.M.; Carroll, K.C.; Liao, J.C.; Wang, T.H. Droplet-Based Single-Cell Measurements of 16S rRNA Enable Integrated Bacteria Identification and Pheno-Molecular Antimicrobial Susceptibility Testing from Clinical Samples in 30 min. *Adv. Sci.* **2021**, *8*, 2003419. [[CrossRef](#)]
7. Hummer, D.; Kurth, F.; Naredi-Rainer, N.; Dittrich, P.S. Single cells in confined volumes: Microchambers and microdroplets. *Lab Chip* **2016**, *16*, 447–458. [[CrossRef](#)]
8. Brower, K.K.; Khariton, M.; Suzuki, P.H.; Still, C., 2nd; Kim, G.; Calhoun, S.G.K.; Qi, L.S.; Wang, B.; Fordyce, P.M. Double Emulsion Picoreactors for High-Throughput Single-Cell Encapsulation and Phenotyping via FACS. *Anal. Chem.* **2020**, *92*, 13262–13270. [[CrossRef](#)]
9. Kaspar, O.; Koyuncu, A.H.; Pittermannova, A.; Ulbrich, P.; Tokarova, V. Governing factors for preparation of silver nanoparticles using droplet-based microfluidic device. *Biomed. Microdevices* **2019**, *21*, 88. [[CrossRef](#)]
10. Frenz, L.; El Harrak, A.; Pauly, M.; Begin-Colin, S.; Griffiths, A.D.; Baret, J.C. Droplet-based microreactors for the synthesis of magnetic iron oxide nanoparticles. *Angew. Chem. Int. Ed. Engl.* **2008**, *47*, 6817–6820. [[CrossRef](#)]
11. James, M.; Revia, R.A.; Stephen, Z.; Zhang, M. Microfluidic Synthesis of Iron Oxide Nanoparticles. *Nanomaterials* **2020**, *10*, 2113. [[CrossRef](#)]
12. Damiati, S. In Situ Microfluidic Preparation and Solidification of Alginate Microgels. *Macromol. Res.* **2020**, *28*, 1046–1053. [[CrossRef](#)]
13. Pittermannova, A.; Ruberova, Z.; Lizonova, D.; Hubatova-Vackova, A.; Kaspar, O.; Zadrazil, A.; Kral, V.; Pechar, M.; Pola, R.; Bibete, J.; et al. Functionalized hydrogel microparticles prepared by microfluidics and their interaction with tumour marker carbonic anhydrase IX. *Soft. Matter.* **2020**, *16*, 8702–8709. [[CrossRef](#)]
14. Moreira, A.; Carneiro, J.; Campos, J.B.L.M.; Miranda, J.M. Production of hydrogel microparticles in microfluidic devices: A review. *Microfluid. Nanofluid.* **2021**, *25*, 1–24. [[CrossRef](#)]
15. Malsch, D.; Kielpinski, M.; Merthan, R.; Albert, J.; Mayer, G.; Kohler, J.M.; Susse, H.; Stahl, M.; Henkel, T. μ PIV-Analysis of Taylor flow in micro channels. *Chem. Eng. J.* **2008**, *135*, 166–172. [[CrossRef](#)]
16. Kim, P.; Kwon, K.W.; Park, M.C.; Lee, S.H.; Kim, S.M.; Suh, K.Y. Soft lithography for microfluidics: A review. *Biochip J.* **2008**, *2*, 1–11.
17. Wang, Y.; Dimitrakopoulos, P. Low-Reynolds-number droplet motion in a square microfluidic channel. *Theor. Comput. Fluid Dyn.* **2012**, *26*, 361–379.
18. Wong, H.; Radke, C.J.; Morris, S. The motion of long bubbles in polygonal capillaries Part. 1. Thin films. *J. Fluid Mech.* **1995**, *292*, 71–94. [[CrossRef](#)]
19. Wong, H.; Radke, C.J.; Morris, S. The motion of long bubbles in polygonal capillaries Part. 2. Drag, fluid pressure and fluid flow. *J. Fluid Mech.* **1995**, *292*, 95–110.
20. Rao, S.S.; Wong, H. The motion of long drops in rectangular microchannels at low capillary numbers. *J. Fluid Mech.* **2018**, *852*, 60–104. [[CrossRef](#)]
21. Fuerstman, M.J.; Lai, A.; Thurlow, M.E.; Shevkoplyas, S.S.; Stone, H.A.; Whitesides, G.M. The pressure drop along rectangular microchannels containing bubbles. *Lab Chip* **2007**, *7*, 1479–1489. [[CrossRef](#)]
22. Ma, S.; Sherwood, J.M.; Huck, W.T.S.; Balabani, S. On the flow topology inside droplets moving in rectangular microchannels. *Lab Chip* **2014**, *14*, 3611–3620. [[CrossRef](#)]
23. Kinoshita, H.; Kaneda, S.; Fujii, T.; Oshima, M. Three-dimensional measurement and visualization of internal flow of a moving droplet using confocal micro-PIV. *Lab Chip* **2007**, *7*, 338–346. [[CrossRef](#)]
24. Oishi, M.; Kinoshita, H.; Fujii, T.; Oshima, M. Simultaneous measurement of internal and surrounding flows of a moving droplet using multicolour confocal micro-particle image velocimetry (micro-PIV). *Meas. Sci. Technol.* **2011**, *22*, 105401. [[CrossRef](#)]
25. Mießner, U.; Helmers, T.; Lindken, R.; Westerweel, J. μ PIV measurement of the 3D velocity distribution of Taylor droplets moving in a square horizontal channel. *Exp. Fluids* **2020**, *61*, 1–17. [[CrossRef](#)]
26. Jakiela, S.; Korczyk, P.M.; Makulska, S.; Cybulski, O.; Garstecki, P. Discontinuous transition in a laminar fluid flow: A change of flow topology inside a droplet moving in a micron-size channel. *Phys. Rev. Lett.* **2012**, *108*, 134501. [[CrossRef](#)]
27. Liu, Z.; Zhang, L.; Pang, Y.; Wang, X.; Li, M. Micro-PIV investigation of the internal flow transitions inside droplets traveling in a rectangular microchannel. *Microfluid. Nanofluid.* **2017**, *21*, 180. [[CrossRef](#)]
28. Li, M.; Liu, Z.; Pang, Y.; Yan, C.; Wang, J.; Zhao, S.; Zhou, Q. Flow topology and its transformation inside droplets traveling in rectangular microchannels. *Phys. Fluids* **2020**, *32*, 052009.
29. Kovalev, A.V.; Yagodnitsyna, A.A.; Bilsky, A.V. Flow hydrodynamics of immiscible liquids with low viscosity ratio in a rectangular microchannel with T-junction. *Chem. Eng. J.* **2018**, *352*, 120–132. [[CrossRef](#)]
30. Leong, C.M.; Gai, Y.; Tang, S.K.Y. Internal flow in droplets within a concentrated emulsion flowing in a microchannel. *Phys. Fluids* **2016**, *28*, 112001. [[CrossRef](#)]
31. Baroud, C.N.; Gallaire, F.; Dangla, R. Dynamics of microfluidic droplets. *Lab Chip* **2010**, *10*, 2032–2045. [[CrossRef](#)]
32. Luo, Z.Y.; Shang, X.L.; Bai, B.F. Marangoni effect on the motion of a droplet covered with insoluble surfactant in a square microchannel. *Phys. Fluids* **2018**, *30*, 077101. [[CrossRef](#)]

33. Luo, Z.Y.; Shang, X.L.; Bai, B.F. Effect of soluble surfactant on the motion of a confined droplet in a square microchannel. *Phys. Fluids* **2019**, *31*, 117104.
34. Dukhin, S.S.; Kovalchuk, V.I.; Gochev, G.G.; Lotfi, M.; Krzan, M.; Malysa, K.; Miller, R. Dynamics of Rear Stagnant Cap formation at the surface of spherical bubbles rising in surfactant solutions at large Reynolds numbers under conditions of small Marangoni number and slow sorption kinetics. *Adv. Colloid Interface Sci.* **2015**, *222*, 260–274. [[CrossRef](#)]
35. Pesci, C.; Weiner, A.; Marschall, H.; Bothe, D. Computational analysis of single rising bubbles influenced by soluble surfactant. *J. Fluid Mech.* **2018**, *856*, 709–763. [[CrossRef](#)]
36. Palaparthi, R.; Papageorgiou, D.T.; Maldarelli, C. Theory and experiments on the stagnant cap regime in the motion of spherical surfactant-laden bubbles. *J. Fluid Mech.* **2006**, *559*, 1–44. [[CrossRef](#)]
37. Baret, J.C.; Kleinschmidt, F.; El Harrak, A.; Griffiths, A.D. Kinetic aspects of emulsion stabilization by surfactants: A microfluidic analysis. *Langmuir* **2009**, *25*, 6088–6093. [[CrossRef](#)]
38. Aksenenko, E.V. *Software Tools to Interpret the Thermodynamics and Kinetics of Surfactant Adsorption, in Surfactants—Chemistry, Interfacial Properties and Application*; Fainerman, V.B., Moebius, D., Miller, R., Eds.; Elsevier: Amsterdam, The Netherlands, 2001.
39. Aksenenko, E.V. Adsorption Software. Available online: <http://www.thomascat.info/Scientific/adso/adso.htm> (accessed on 15 June 2021).
40. Pirbodaghi, T.; Vigolo, D.; Akbari, S.; de Mello, A. Investigating the fluid dynamics of rapid processes within microfluidic devices using bright-field microscopy. *Lab Chip* **2015**, *15*, 2140–2144. [[CrossRef](#)]
41. Buzzaccaro, S.; Secchi, E.; Piazza, R. Ghost particle velocimetry: Accurate 3D flow visualization using standard lab equipment. *Phys. Rev. Lett.* **2013**, *111*, 048101. [[CrossRef](#)]
42. Riccomi, M.; Alberini, F.; Brunazzi, E.; Vigolo, D. Ghost Particle Velocimetry as an alternative to μ PIV for micro/milli-fluidic devices. *Chem. Eng. Res. Des.* **2018**, *133*, 183–194. [[CrossRef](#)]
43. Kovalchuk, N.M.; Chowdhury, J.; Schofield, Z.; Vigolo, D.; Simmons, M.J.H. Study of drop coalescence and mixing in microchannel using Ghost Particle Velocimetry. *Chem. Eng. Res. Des.* **2018**, *132*, 881–889. [[CrossRef](#)]
44. Schneider, C.A.; Rasband, W.S.; Eliceiri, K.W. NIH Image to ImageJ: 25 years of image analysis. *Nat. Methods* **2012**, *9*, 671–675. [[CrossRef](#)]
45. Thielicke, W.; Stamhuis, E.J. PIVlab—Towards User-friendly, Affordable and Accurate Digital Particle Image Velocimetry in MATLAB. *J. Open. Res. Softw.* **2014**, *2*, e30. [[CrossRef](#)]
46. Mucic, N.; Javadi, A.; Kovalchuk, N.M.; Aksenenko, E.V.; Miller, R. Dynamics of interfacial layers-experimental feasibilities of adsorption kinetics and dilational rheology. *Adv. Colloid Interface Sci.* **2011**, *168*, 167–178. [[CrossRef](#)]
47. Abdel-Rahem, R.A. Influence of Glycerol and Temperature on the Phase Behavior and Micellization of CTAB and SDS in Aqueous Solutions. *J. Dispers. Sci. Technol.* **2013**, *34*, 932–940.
48. Kovalchuk, N.M.; Roumpea, E.; Nowak, E.; Chinaud, M.; Angeli, P.; Simmons, M.J.H. Effect of surfactant on emulsification in microchannels. *Chem. Eng. Sci.* **2018**, *176*, 139–152. [[CrossRef](#)]
49. Bağ, A.; Podgórska, W. Interfacial and surface tensions of toluene/water and air/water systems with nonionic surfactants Tween 20 and Tween 80. *Colloids Surf. A Physicochem. Eng. Asp.* **2016**, *504*, 414–425. [[CrossRef](#)]
50. Stubenrauch, C.; Fainerman, V.B.; Aksenenko, E.V.; Miller, R. Adsorption Behavior and Dilational Rheology of the Cationic Alkyl Trimethylammonium Bromides at the Water/Air Interface. *J. Phys. Chem.* **2005**, *109*, 1505–1509.
51. Fainerman, V.B.; Lylyk, S.V.; Aksenenko, E.V.; Liggieri, L.; Makievski, A.V.; Petkov, J.T.; Yorke, J. Adsorption layer characteristics of Triton surfactants. *Colloids Surf. A Physicochem. Eng. Asp.* **2009**, *334*, 8–15. [[CrossRef](#)]
52. Ferri, K.J.; Stebe, K.J. Which surfactants reduce surface tension faster? A scaling argument for diffusion-controlled adsorption. *Adv. Colloid. Interface. Sci.* **2000**, *85*, 61–97.
53. Wilke, C.R.; Chang, P. Correlation of diffusion coefficients in dilute solutions. *AIChE. J.* **1955**, *1*, 264–270. [[CrossRef](#)]
54. Poling, B.E.; Prausnitz, J.M.; O’Connell, J.P. *Properties of Gases and Liquids*, 5th ed.; McGraw-Hill Education: New York, NY, USA, 2001.
55. Perkins, L.R.; Geankoplis, C.J. Molecular diffusion in a ternary liquid system with the diffusing component dilute. *Chem. Eng. Sci.* **1969**, *24*, 1035–1042. [[CrossRef](#)]
56. Joos, P. *Dynamic Surface Phenomena*; VSP: Utrecht, The Netherlands, 1999.
57. Levich, V.G. *Physicochemical Hydrodynamics*; Prentice-Hall: New Jersey, NJ, USA, 1962.